

The impact of initial tracer profile on the exchange and on-shelf distribution of tracers induced by a submarine canyon

Karina Ramos-Musalem^{1*} and Susan E. Allen¹

¹Department of Earth, Ocean and Atmospheric Sciences, University of British Columbia, Vancouver,
British Columbia, Canada

Key Points:

- A pool of low oxygen and high DIC and nutrients is formed on the shelf bottom, downstream of the canyon.
- Pool size is a function of on-shelf canyon-induced tracer flux and the geometry of the initial tracer profile.
- Estimating tracer flux from water flux can have an associated error of up to 40% for profiles with a steep gradient near shelf-break depth.

*2020-2207 Main Mall, Vancouver, BC Canada V6T 1Z4

Corresponding author: Karina Ramos-Musalem, kramosmu@eoas.ubc.ca

Abstract

Submarine canyons enhance cross-shelf mass exchanges, which are a key component of on-shelf nutrient budgets and biogeochemical cycles. Previous studies assume that canyon-induced tracer flux onto the shelf only depends on canyon-induced water upwelling. This paper investigates the validity of this dependence for nutrients, carbon and dissolved gasses. To estimate the canyon-induced tracer upwelling flux and its spatial distribution on the shelf, we performed numerical experiments simulating an upwelling event near an idealized canyon, adding 10 passive tracers with initial profiles representing nutrients, carbon and dissolved gasses. This paper presents a scaling estimate for canyon-induced tracer upwelling and for the on-shelf distribution of a given tracer.

We find that tracer upwelling depends on the vertical local mean of the initial vertical tracer gradient within the canyon, the depth of upwelling and the upwelling flux. We identify a pool of low oxygen and high nutrient concentration, methane, dissolved inorganic carbon and total alkalinity on the shelf bottom, downstream of the canyon. The downstream extension of the pool of low oxygen water depends on the onshore flux of water through the canyon and the oxygen profile. This canyon-induced distribution of tracers has the potential to impact demersal and benthic ecosystems by lowering dissolved oxygen levels and spreading corrosive waters along the shelf.

Plain Language Summary

Submarine canyons are topographical features that cut across the continental shelves all around the world. Close to the continental shelf, currents usually flow following the depth contours of the ocean bottom. Near submarine canyons, however, currents are bent by the topography and vertical flows occur more readily. This allows deep nutrient-rich, oxygen-depleted water to reach closer to the surface, where biomass tends to be more abundant, making canyons hot spots for marine life. This work uses computer simulations of ocean circulation to investigate the amount of nutrients, oxygen, carbon and other substances that currents through a submarine canyon deliver from deeper to shallower waters, and it provides mathematical formulas to calculate such fluxes.

We find that these fluxes depend on the initial distribution of the substances in the water column and the strength of the currents generated by the canyon. We also identify a pool of deep water (high content of nutrients, low oxygen levels, high in carbon

and alkalinity) sitting on the bottom of the shelf, near the canyon. We show that this pool can be large enough to impact the shelf-bottom ecosystem by lowering dissolved oxygen levels and spreading corrosive waters along the shelf.

1 Introduction

Submarine canyons constitute 1.2% of the world’s continental margins (Harris et al., 2014). These ubiquitous topographic features connect the continental shelf and the deep ocean at different depths as they serve as pathways for water and solutes such as nutrients and oxygen, sediments, organic matter, and marine debris (Allen & Durrieu de Madron, 2009; Puig et al., 2014). Submarine canyons are sites where regional circulation is strongly influenced by topographically-induced dynamics (e.g. B. M. Hickey, 1995; Allen et al., 2001; Kämpf, 2010).

Cross-shelf exchange of water and passive tracers, such as dissolved oxygen, nutrients and carbon, is limited as homogeneous, geostrophic flow is restricted to follow isobaths along the continental shelf (Taylor-Proudman Theorem) (e.g. Brink, 1998). Deep ocean exchange occurs only when ageostrophic dynamics are induced. Ageostrophic dynamics are induced in submarine canyons because the Rossby number is higher in these regions relative to the adjacent slopes, indicating that advection of momentum is an important driver of flow near submarine canyons (Allen & Durrieu de Madron, 2009).

Submarine canyons are often biodiversity hotspots as local flows trap organic matter in canyons, enhancing overall ecosystem biomass (Allen et al., 2001; De Leo et al., 2010; Fernandez-Arcaya et al., 2017; Santora et al., 2018). Both the distribution and on-shelf inventory of tracers (such as nutrients and oxygen) can have relevant biological consequences for the shelf system. Upwelling of hypoxic waters with high CO_2 concentrations can displace or kill benthic organisms; however, high nutrients in upwelled waters can trigger productivity (Breitburg et al., 2018). In the past 10 years, corrosive water (undersaturated with respect to aragonite) has been observed covering larger areas of the shelf and reaching shallower depths than normal on the West Coast of North America (Feely et al., 2008). Moreover, in upwelling regions, advection of oxygen-depleted waters and local biological consumption spiked by high productivity are important drivers of hypoxic events on the shelf (Connolly et al., 2010) and both mechanisms decrease pH on the shelf. On the West Coast of Vancouver Island, sediment-associated processes dom-

76 inate the consumption of oxygen and release of inorganic carbon to the bottom waters
 77 over the shelf (Bianucci et al., 2011).

78 Hypoxic events are common in the Washington shelf and advection of oxygen-depleted
 79 waters through coastal upwelling is a key mechanism to generate such events (Connolly
 80 et al., 2010). A recent numerical study of the coast of Washington State found that changes
 81 in near-shelf bottom oxygen concentrations in the presence of three nearby canyons matched
 82 levels of hypoxia in the region. These changes were large enough to have an ecological
 83 impact if compared to levels of severe hypoxia associated with mortality in marine or-
 84 ganisms. Moreover, it has been reported that on the west coast of the United States small
 85 changes in dissolved oxygen concentrations in already hypoxic waters can cause large changes
 86 in the total and species-specific catch of demersal fish (Keller et al., 2017). In addition,
 87 shoaling of the oxygen minimum zone along eastern ocean boundaries will contribute to
 88 lower concentrations of oxygen on the continental shelf (Whitney et al., 2007).

89 Methane and nitrous-oxide are the most significant greenhouse gases after carbon-
 90 dioxide and water-vapor (IPCC, 2013). On the southern West Coast of Vancouver Is-
 91 land, methane is supplied to the water column mainly from methane seeps and other sed-
 92 imentary processes, while nitrous-oxide is supplied from an off-shelf nitrous oxide max-
 93 imum and from nitrification in the water column (Capelle & Tortell, 2016). The main
 94 on-shelf transport mechanism for methane and nitrous oxide is upwelling, but local to-
 95 pography has also been identified to increase the supply of these tracers onto the shelf
 96 (Capelle & Tortell, 2016).

97 Barkley Canyon and Astoria Canyon are two short (i.e. the canyon head does not
 98 extend close to the coast), dynamically narrow (Rossby radius of deformation is larger
 99 than the canyon width), shelf canyons located on the West Vancouver Island Shelf (48.25° ,
 100 126.16°) and the Washington Shelf (46.25° , -124.50°), respectively. The flow dynamics
 101 in Barkley Canyon and Astoria Canyon have been well studied (Allen et al., 2001; B. M. Hickey,
 102 1997) and they are representative of the canyons on the Northwest coast of North Amer-
 103 ica. Both canyons experience upwelling favourable conditions during the summer as part
 104 of the California Upwelling System (B. M. Hickey, 1989, 1997; Allen et al., 2001; Con-
 105 nolly & Hickey, 2014) although wind stress is weaker than further south (B. M. Hickey,
 106 1989). Near-surface equatorward flow is present over the slope during April-October, al-
 107 though the California Undercurrent develops below shelf break depth over the slope dur-

ing late summer (B. Hickey, 1998). Local wind forcing is not the only important factor determining event-scale variations on the shelf. In summer, first-mode coastal trapped waves generated further south explain much of the several-day scale variability (Battisti & Hickey, 1984). Passing coastal trapped waves can relax or reverse poleward flow in the undercurrent (Connolly & Hickey, 2014). Therefore, canyon-enhanced upwelling can still occur during late summer (Connolly & Hickey, 2014).

Astoria Canyon is wider at the mouth (15.7 km vs 13.0 km) but narrower at mid length (8.0 km vs 8.3 km), it is longer than Barkley Canyon (21.8 km vs. 6.4 km), and it has a shallower shelf break (150 m vs. 200 m). (Figure 1 a, b). Using typical summer conditions Allen and Hickey (2010) estimate that the Rossby number $R_W = U/fW_s$ is larger for Astoria Canyon than for Barkley Canyon (0.12 vs 0.07), where U is a characteristic scale for the incoming flow into the canyon, f is the Coriolis parameter and W_s the width at mid length; the Burger number $Bu = NH_s/fW_s$, where N is the buoyancy frequency and H_s the shelf break depth, is slightly larger for Astoria Canyon than for Barkley Canyon (1.2 vs 1.1). Higher R_W within the canyon leads to higher canyon-induced upwelling flux and deeper depth of upwelling, while lower Bu has a similar effect (Allen & Hickey, 2010; Howatt & Allen, 2013). These canyons will be used as motivation to our experimental configuration and interpretation of results.

There has been extensive research on the upwelling circulation within submarine canyons (e.g. Allen & Hickey, 2010; Howatt & Allen, 2013; Freeland & Denman, 1982; Klinck, 1996; Kämpf, 2007). However, the relationship between flow dynamics in submarine canyons and their contribution to biogeochemical budgets and on-shelf distribution of tracers on the shelf is less understood. In previous numerical work on an idealized short, narrow canyon, it was shown that a passive tracer is upwelled onto the shelf on the downstream side of the canyon (Ramos-Musalem & Allen, 2019, hereafter RA2019). The upwelled water spreads out on the shelf, downstream of the rim and generates a region of relatively larger tracer concentration near the bottom. Enhanced mixing within the canyon can impact the flow in two ways: first, it increases the upwelling flow by weakening the stratification below rim depth due to isopycnal stretching; second, it increases the tracer concentration near rim depth, upwelling water with higher concentration than in the case with uniform diffusivity. These combined effects can increase the tracer upwelling flux by 27% in a submarine canyon with enhanced diffusivity 3 orders of magnitude larger than background (along adjacent shelves) values. Here, the task is to ex-

plain the impact of the canyon on the on-shelf, near bottom distribution of tracers. To that end, in this paper we model an upwelling event on a shelf incised by an idealized submarine canyon using realistic initial vertical profiles of 10 different passive tracers (nutrients, dissolved gases, carbon, and oxygen), and we analyse the canyon-induced upwelling flux, net on-shelf transport, and final on-shelf distribution of these tracers.

This paper identifies the effect of the initial geometry of a tracer profile on the on-shelf distribution of that tracer after an upwelling event and discusses the impact of the canyon on the oxygen and carbon levels near the adjacent shelf bottom.

We explain the numerical configuration and experiments in section 2; we describe the flow dynamics of the canyon in section 3.1; we report on the cross-shelf transport, on-shelf distribution and canyon-induced upwelling of tracers in sections 3.2, 3.3, 3.4, respectively; we find scaling estimates for the amount of tracer upwelled onto the shelf by the canyon and the on-shelf distribution of tracer in section 4, and finally we discuss and summarize our findings in section 5.

2 Methods

2.1 The model

We use the *Massachusetts Institute of Technology general circulation model* (MIT-gcm) (Marshall et al., 1997) with a similar configuration to RA2019 but in this work we initialize ten different passive tracers instead of one. The model simulations use a bathymetry which consists of a sloping continental shelf cut by an idealized submarine canyon and force shelf currents that flow southward from the northern side of the domain (i.e. in the upwelling-favourable direction), parallel to the shelf (Figure 1). The simulations start from rest and have a run duration of 9 days, consistent with the dominant current variability time scale in the region of 3-10 days (B. M. Hickey, 1989; B. M. Hickey & Banas, 2003). A shelf current is spun-up by applying an along-shelf body force directed southward on every cell of the domain to produce similar effects as those that result from changing the rotation rate of a rotating table (Spurgin & Allen, 2014). The body forcing ramps up linearly during the first simulation day, remains constant for the second simulation day, and ramps down to a minimum forcing strength on the third day, after which it remains constant to avoid spin-down of the shelf currents. This forcing generates a deeper shelf current, less focused on the surface, than the coastal jet generated by wind-forced

models. This is an important feature given that the ambient currents at shelf-break depth determine the strength of canyon-induced upwelling (Mirshak & Allen, 2005; Kämpf, 2007; Allen & Hickey, 2010). These upwelling-favourable conditions have been observed in Barkley Canyon (Allen et al., 2001) and Astoria Canyon (B. M. Hickey, 1997). Additional evidence is provided in the Supplementary Information (Figures S2 and S3).

The domain is 280 km alongshelf and 110 km across-shelf divided in 616x360 cells horizontally. The canyon axis is located 60 km away from the northern boundary and 220 km away from the southern boundary. The cell width increases smoothly alongshelf and cross-shelf, from 115 m over the canyon to 437 m at the west boundary, and to 630 m at a distance of 60 km upstream and downstream of the canyon and then is uniform to the downstream boundary. Vertically, the domain is divided into 104 z-levels spanning a maximum depth of 1200 m, with grid sizes increasing smoothly from 5 m (surface to 260 m) to 20 m at depth. The time step used was 40 s, with no distinction between baroclinic and barotropic time steps. The experiments ran in hydrostatic mode. Some runs were also repeated in non-hydrostatic mode with no significant differences in the results.

We ran experiments with two different idealized canyons with geometric parameters (Figure 1) similar to those of Barkley Canyon and Astoria Canyon, respectively. The bathymetries were constructed from a hyperbolic tangent function.

The domain has open boundaries at the coast (east) and deep ocean (west). Open boundaries use Orlanski radiation conditions without a sponge layer. At the bottom, boundary conditions are free-slip using a quadratic bottom drag with coefficient 0.002. At the vertical walls of the model bathymetry steps, boundary conditions are free-slip. North and south boundaries are periodic. The alongshelf width of the model domain is sufficiently large to avoid the recirculation of water through the canyon. However, barotropic Kelvin waves, first and second mode baroclinic Kelvin waves, and long wavelength shelf waves do recirculate through the domain as in previous studies with similar configurations (e.g. She & Klinck, 2000; Dinniman & Klinck, 2002, RA2019). Subinertial shelf waves of wavelength likely to be excited by the canyon ($\lambda \approx 2W_m$) (Zhang & Lentz, 2017) are too slow to recirculate with speeds AST 0.07 ms^{-1} , BAR 0.04 ms^{-1} , ARGO -0.04 ms^{-1} and PATH 0.02 ms^{-1} against the mean incoming flow (Calculated using Brink, 2006).

As in a previous study (RA2019), we use the GMREDI package included in MIT-gcm for diffusing tracers. We use the scheme for isopycnal diffusion (Redi, 1982) but did not use the skew-flux parametrization (Gent & McWilliams, 1990). In turn, the vertical effective diffusivity on the tracer is determined by the prescribed vertical eddy diffusivity $K_v = 10^{-5} \text{ m}^2\text{s}^{-1}$, the tilting of isopycnals via the Redi scheme (vertical contribution) and the diffusivity due to the advection scheme, which is a 3rd order, flux-limited scheme that treats space and time discretizations together (direct space time) and uses non-linear interpolation (non-linear scheme) (Marshall et al., 1997).

Four types of experiments were conducted (Table 1) using either Astoria-like or Barkley-like bathymetry and either idealized or realistic profiles of temperature and salinity. The control runs for Astoria-like and Barkley-like bathymetry (AST and BAR in Table 1) use initial fields of temperature and salinity that vary linearly in the vertical (Figure 1 d,e). To compare the effect of the canyon on tracers in a more realistic scenario, we did two runs using temperature and salinity profiles from observations (ARGO and PATH runs in Table 1). For ARGO (Astoria-like bathymetry) we used temperature and salinity profiles from ARGO platform 5903601 (cast 94, 2014-05-31) at the mouth of Astoria Canyon. These data were collected and made freely available by the International Argo Program and the Coriolis project (<http://www.argo.ucsd.edu>, <https://www.coriolis.eu.org>). For PATH (Barkley-like bathymetry) we used temperature and salinity profiles from the Pathways Cruise (Klymak et al., 2013) (see section 2.2) averaged along canyon axis stations. The circulation around both canyons using realistic stratification is similar to that around the corresponding counterparts with linear stratification, except near the surface where the effect of the canyon topography on the flow is less pronounced. In all runs temperature and salinity are initially homogeneous horizontally. Notably, for all aforementioned runs (hereafter referred to as canyon cases), we conducted corresponding runs with identical conditions except that the bathymetry includes only a shelf and slope which are not incised by a canyon (hereafter referred to as no-canyon cases).

2.2 Tracers

In this paper we expand the results in RA2019 for realistic tracer profiles with different geometric features from a linear tracer (Figure 2 and Table 2). To do this, ten passive tracers were introduced from the beginning of the simulations with vertical profiles of salinity, nitrate, dissolved silicon (DS), phosphate, dissolved oxygen, dissolved inor-

Table 1. *Experiment Parameters*

Experiment	Bathymetry	Active tracers	N_0 (10^{-3} s^{-1})	f (10^{-4} s^{-1})	U (ms^{-1})
AST	Astoria	linear	5.5	1.00	0.30
BAR	Barkley	linear	5.5	1.00	0.30
ARGO	Astoria	ARGO float	9.9	1.05	0.33
PATH	Barkley	Pathways	3.8	1.08	0.29

Note. All experiments were initialized with 10 passive tracers (Table 2). Temperature and salinity profiles (active tracers) vary between runs. The stratification for ARGO and PATH experiments corresponds to the mean stratification through the upwelling depth (about 100 m below head depth) following Allen and Hickey (2010). For every run there is a corresponding no-canyon case.

ganic carbon (DIC) and total alkalinity collected during the Pathways Cruise in summer, 2013 in Barkley Canyon (Klymak et al., 2013); with vertical profiles of methane and nitrous oxide sampled along Line C, upstream of Barkley Canyon (Figure S1 supplementary material) in May and September from 2012 and 2013 (Capelle & Tortell, 2016) as well as a linear tracer. The Pathways campaign took place from August 18th to September 18th, 2013 on board of the R/V Falkor. The campaign included 7 Conductivity-Temperature-Pressure sensors (CTD) stations along the axis of Barkley Canyon. Four of these stations also had bottle samples for nitrate, phosphate, oxygen, dissolved silicon (DS), dissolved inorganic carbon (DIC) and total alkalinity. Vertical profiles measured at each station were interpolated and averaged to find a mean profile for the canyon region (Figure 2).

2.3 Transport sections

To determine the pathways of water and tracers onto the shelf, we calculate their cross-shelf (CS) and vertical transports. We define CS transport of water as the volume of water per unit time that flows across the vertical planes (CS1-CS6) that extend from the shelf break in the no-canyon case to the surface (Figure 1 a, c), while vertical transports flow across the horizontal plane (LID) delimited by the shelf break depth in the

Table 2. *Initial Tracer Concentration and Tracer Gradient at Shelf Break Depth*

Tracer	Astoria-like Bathymetry		Barkley-like Bathymetry	
	C_{sb}	$\partial_z C$	C_{sb}	$\partial_z C$
	(μM)	($\mu M m^{-1}$)	(μM)	($\mu M m^{-1}$)
Linear	7.2	3.6×10^{-2}	9.0	3.6×10^{-2}
Oxygen (Dissolved oxygen)	1.1×10^2	-2.9×10^{-1}	86.6	-0.36
Nitrate	32.6	3.8×10^{-2}	34.9	4.4×10^{-2}
DS (Dissolved Silicon)	47.6	8.5×10^{-2}	52.5	0.11
Phosphate	2.2	2.2×10^{-3}	2.4	2.9×10^{-3}
DIC (Dissolved Inorganic Carbon)	2.3×10^3	0.67	2.3×10^3	0.25
Alkalinity	2.3×10^3	0.17	2.3×10^3	0.17
Nitrous-oxide	2.8×10^{-2}	4.7×10^{-5}	2.8×10^{-2}	6.4×10^{-6}
Methane	1.8×10^{-2}	2.4×10^{-4}	3.6×10^{-2}	2.3×10^{-4}

Note. Initial concentration (C_{sb}) and vertical gradient at shelf break depth ($\partial_z C$) for all tracers initialized in the four runs analysed in this paper.

canyon case and the canyon walls (Figure 1 a, c). We define the net or total water and tracer transport onto the shelf as the temporal mean during the advective phase (days 4-9) of the sum of the water and tracer transports through cross sections CS1-CS6 and LID. We define the vertical water transport and tracer transport onto the shelf as the mean transport through LID during the advective phase (days 4-9). The flux and transport of tracers are derived as model diagnostics. The effect of the canyon on cross-shelf fluxes is defined as the flux anomaly between canyon and no-canyon cases (canyon contribution). Negative transports generally mean that either water or tracer is leaving the shelf; it is only near the shelf bottom, where shelf upwelling is onshore, that negative transports mean that transport for the no-canyon case is larger than in the canyon case.

2.4 Upwelling quantification

Upwelled water on the shelf has been estimated previously by finding water originally below shelf-break depth based on its salinity or concentration of a linear tracer (Howatt

& Allen, 2013, RA2019). We take a different approach to calculate the upwelling flux of water $\Phi(t)$ by calculating the cross-shelf transport of water through cells along the shelf-break wall (CS2-CS5) and LID section (Figure 1a, 1c), with concentration of the linear tracer C larger or equal than the initial concentration at shelf break depth C_{sb} . This algorithm only considers cross-shelf exchange of water that was originally below shelf-break depth by selecting cells with a concentration of linear tracer higher or equal than C_{sb} :

$$\Phi(t) = \sum_i v_i(t) a_i \text{ where } C_i(t) > C_{sb} + \sum_j w_j(t) a_j \text{ where } C_j(t) > C_{sb}, \quad (1)$$

where the first sum is over cells on sections (CS2-CS5) and the second sum over cells in the horizontal section LID, v_i is the cross-shelf velocity at the i -th cell on the shelf wall (CS2-CS5), a_i its area and C_i its concentration of linear tracer, w_i is the vertical velocity of the i -th cell on section LID, a_j its area and C_j its concentration of linear tracer.

Once the cells with upwelled water on the cross-shelf sections CS2-CS5 and LID have been identified, we calculate the flux of all 10 tracers through those selected cells. For any tracer with concentration \mathcal{C} , the upwelling tracer flux Φ_{Tr} is given by

$$\Phi_{Tr}(t) = \sum_i v_i(t) \mathcal{C}_i(t) a_i \text{ where } C_i(t) > C_{sb} + \sum_j w_j(t) \mathcal{C}_j(t) a_j \text{ where } C_j(t) > C_{sb}, \quad (2)$$

where v_i , w_j are the cross-shelf and vertical velocities at the i -th and j -th cells on the shelf wall (CS2-CS5) and LID sections, respectively; a_i and a_j their areas; C_i , C_j their concentration of linear tracer; and \mathcal{C}_i , \mathcal{C}_j their tracer concentration, respectively.

We calculate the total amount of tracer mass for any given tracer on shelf at a given time $\mathcal{M}(t)$, by integrating the volume of each cell on the shelf multiplied by its tracer concentration $C(t)$:

$$\mathcal{M}(t) = \sum_{shelf} \mathcal{C}(t) \Delta V, \quad (3)$$

where ΔV is the volume of a cell on the shelf and \mathcal{C} its concentration. This includes cells from the bottom of the shelf all the way to the surface and from the shelf break to the coast. $\mathcal{M}(t)$ reflects all processes and exchanges of mass at any depth and from any kind of water; it is the total inventory of tracer on shelf.

3 Results

3.1 Canyon upwelling and circulation

The model starts from rest. During the first day, body forcing ramps up linearly; it is kept constant for a day and ramps down to a lower value, just enough to prevent the generated slope current from spinning down for the rest of the simulation. For the first four days the circulation within the canyon is strongly time-dependent (time dependent phase) and its response is linear (Allen, 1996) with the forcing. After day 4, the circulation is dominated by advection (advective phase). A rim depth eddy forms, circulation is cyclonic within the canyon and water upwells close to the canyon head, on the downstream side. The circulation and upwelling response to the forcing is similar for both bathymetries, Astoria Canyon and Barkley Canyon and both idealized and realistic temperature and salinity profiles. These results follow previous descriptions of upwelling in short canyons (e.g. Allen et al., 2001; Waterhouse et al., 2009; Howatt & Allen, 2013, RA2019).

The main characteristics of canyon upwelling and circulation are more intense for Astoria Canyon than for Barkley Canyon. Compared to Astoria runs, Barkley runs include not only a shorter, narrower canyon, but also a deeper shelf break, both which reduce near-surface effects in Barkley Canyon runs. The mean velocities of the coastal jet and slope current are higher in Astoria Canyon than in Barkley Canyon (Figure 3c, g) but the magnitude of the incoming velocity U (i.e. the flow that encounters the canyon on its upstream rim) is the same, by construction, for both canyons (Figure 3i). The incoming velocity U is the alongshore velocity upstream of the canyon, above the bottom boundary layer, which has been identified as the relevant velocity scale for canyon-induced upwelling (Allen & Hickey, 2010). The incoming shelf flow veers towards the canyon head when crossing over the canyon and slightly offshore on the downstream side of the canyon. This effect is more intense for Astoria Canyon runs than for Barkley Canyon runs (Figure 3a, e).

Near rim depth, on the upstream side of the canyon, incoming water falls into the canyon, stretching the water column and generating cyclonic vorticity (Allen et al., 2001). This same mechanism triggers a significant standing topographic Rossby wave in the AST experiment (not shown) (Kämpf, 2018).

Upwelling within the canyon is forced by an unbalanced horizontal pressure gradient between canyon head and canyon mouth (Freeland & Denman, 1982). In response, a balancing, baroclinic pressure gradient is generated by rising isopycnals toward the canyon head (Figure 3d,h). The advection of the tracer field is similar to the density (Figure 3d,h). Near the canyon rim, pinching of isopycnals occurs on the upstream side (Figure 3 b,f). This well-known feature has been observed in Astoria Canyon (B. M. Hickey, 1997) and numerically simulated (e.g., Howatt & Allen, 2013; Dawe & Allen, 2010).

In the no-canyon case, shelf-break upwelling caused by on-shelf transport in the bottom Ekman layer brings water onto the shelf through a thin band along the shelf bottom (not shown). Elsewhere, above that band, water transport is off-shore. In the presence of a submarine canyon, water is also upwelled through the canyon, mostly on the downstream side of the canyon, as seen from vertical velocities and vertical transport through horizontal cross-section LID (Figure 3a,e,j,k). Water is pushed onto the shelf, above the canyon more strongly closer to the shelf break depth and within the canyon, while shelf upwelling is suppressed just upstream of the canyon because water is redirected to upwell through the canyon (Figure 3j,k). Cross-shelf transport of water is on-shelf through the canyon lid (LID) and above the canyon (CS3), and balanced by the rest of the shelf (CS1,CS2,CS4,CS5,CS6) by mostly off-shelf transport. Small variations in net cross-shelf water transport can be explained by variations in sea surface height. Vertical water transport and CS3 on-shelf transport peak around day 3, when maximum forcing has been reached, and decrease slowly during the advective phase. This pattern is mimicked by off-shelf transport downstream of the canyon with a lag of half day. Water transports are higher through all cross-sections for Astoria Canyon than for Barkley Canyon. The realistic run for Astoria Canyon (ARGO) has weaker water transports than AST and there is little difference between Barkley Canyon (BAR) and its realistic run, PATH, although the former tends to be slightly stronger.

3.2 Cross-shelf transport

In this section we describe the pathways followed by three tracers with the most distinct initial profiles as they are upwelled onto the shelf during an upwelling event: methane, which has a step-like maximum near 150 m, oxygen that decreases with depth, and DIC that increases smoothly with depth. The linear tracer, salinity, nitrate, DS, nitrous-oxide and alkalinity, mimic DIC closely. Tracer transport is on-shelf and strong near shelf bot-

tom and off-shelf and weak above the upwelling band. For tracers that increase with depth this means that higher tracer concentrations are being transported onto the shelf while lower concentrations are exported off the shelf.

Tracer transport onto the shelf occurs mostly above the canyon and through the canyon lid (canyon induced) and right above the shelf break (shelf-break upwelling) (Figure 4 panels a1-e1 and a2-e2). Off-shelf tracer transport occurs downstream of the canyon and above the shelf-break upwelling band both upstream and downstream of the canyon (Figure 4 a1-e1). The main on-shore tracer transport patch and off-shore structure of tracer transport are similar to water transport (Figure 3j, k) but the vertical extent and finer structure depend on the initial tracer profile (Differences between panels a1-e1 and a2-e2 Figure 4). The downstream offshore transport is associated with a stationary topographic Rossby wave, and as such, is very dependent on stratification. We see a different pattern in ARGO (not shown) but the mean flow is still off-shore downstream of the canyon. Due to the downstream vertical structure observed for water and thus, tracer transport, we ran AST in non-hydrostatic mode. For all tracers, the maximum difference between hydrostatic and non-hydrostatic runs is less than 0.3% of the mean transport (not shown).

Considering DIC, tracer transport is onto the shelf through sections CS3 and LID and mostly offshore upstream and downstream of the canyon (sections CS1, CS2, CS4, CS5, CS6) (Figure 4 d1-d6) for all runs. The strong initial on-shore transport induced by the canyon through LID and CS3 is mostly balanced by off-shore transport through CS4 but not completely. Upstream of the canyon there is not much transport either on-shore or offshore but downstream through CS6 the sign of the transport depends on the run we look at.

The net transport of DIC and methane is onto the shelf and higher for Astoria Canyon runs than for Barkley Canyon runs and highest for Astoria Canyon with linear stratification (AST). It is maximum at day 3, when maximum forcing is reached, and then it decreases to be nearly constant after day 4 during the advective phase (Figure 4 d6). This tracer transport pattern is similar for profiles of tracers that increase with depth with varying magnitudes.

Given that oxygen has a decreasing profile, tracer transport is different from the other tracers. Although transport through CS3 and LID is onshore as for the other trac-

Table 3. *Mean and Maximum Net Cross-shelf Tracer Transport*

Exp	Mean NT (10^4 TU)	Mean NT relative to AST (%)	Canyon contribution %	Max NT (10^4 TU)	Max NT relative to AST (%)	Canyon contribution %
AST Oxy	-644.9 ± 26.0	100.0	31.7	-60.6	100.0	36.4
ARGO Oxy	-515.1 ± 16.4	79.9	15.8	-59.7	98.3	32.6
BAR Oxy	-380.7 ± 14.0	59.0	1.9	-35.4	58.3	8.4
PATH Oxy	-429.6 ± 22.6	66.6	5.6	-38.8	63.8	9.3
AST Met	0.19 ± 0.02	100.0	58.5	0.4	100.0	87.4
ARGO Met	0.14 ± 0.01	71.7	42.2	0.3	66.6	80.9
BAR Met	0.14 ± 0.01	71.3	4.6	0.2	46.9	17.5
PATH Met	0.15 ± 0.01	78.0	6.8	0.2	52.4	20.4
AST DIC	1928.1 ± 123.6	100.0	67.9	2377.0	100.0	85.8
ARGO DIC	1433.1 ± 128.1	74.3	61.2	1856.9	78.1	63.6
BAR DIC	664.4 ± 31.0	34.5	20.8	906.7	38.14	34.4
PATH DIC	686.5 ± 36.1	35.6	19.3	981.7	41.30	32.8

Note. In columns 2-4: Mean net transport (NT), Mean NT relative to AST transport and canyon contribution to Mean NT for selected tracers; in columns 5-7: Same as 2-4 but for Maximum net transport (Max NT). Tracer transport units (TU) are $\mu\text{mol kg}^{-1}\text{m}^3\text{s}^{-1}$, $n\text{Mm}^3\text{s}^{-1}$, $\mu\text{mol kg}^{-1}\text{m}^3\text{s}^{-1}$.

ers, there is a larger off-shore contribution from CS4 and CS6 for all runs so net oxygen transport is off-shore throughout the upwelling event. The maximum off-shore transport occurs at day 3 and after day 4 it is mostly constant (Not shown).

We calculate the canyon contribution to net cross-shelf tracer transport by subtracting the net tracer transport calculated for corresponding runs with no-canyon bathymetry (Figure 4a3-c3). The residual from this anomaly is the canyon contribution. We look at the mean net CS transport during the advective phase (Table 3 column 2) and the canyon contribution during that period of time (shown as a percentage in table 3, column 4). Additionally, we compare the mean net tracer transport in a run to the corresponding mean net tracer transport for the Astoria run (AST) (Table 3, column 3).

Net tracer transport is largest in AST followed by ARGO (70-80% of AST). Runs with Barkley Canyon bathymetry have lower net transports for most tracers (BAR 34-71%, PATH 35-78%) except for methane, which is very similar for ARGO, BAR and PATH. This general trend can be explained by the vertical transport and cross-shelf transport of water through CS3 for each run, which are largest for AST, followed by ARGO, PATH and BAR, and carry water with higher tracer concentration than the water that is leaving the shelf. Deviations in the net tracer transport from AST are explained by the initial shape of the tracer profile. Net transport will be closer to zero (like water) the more uniform the tracer profile is, but if the gradient close to the shelf break is large then the transport will be larger. This impact is most evident for methane.

Considering the impact of a canyon on total transport Astoria Canyon's contribution to tracer transport is also larger than Barkley Canyon's (Table 3). This can be explained by canyon upwelling scaling and seen in water transport anomaly. An example of this is that, even though methane transport is similar for all runs, the contribution of Astoria Canyon is 42-58% but Barkley Canyon's is only 4-6%, showing that shelf break upwelling of methane is more important for Barkley Canyon and canyon upwelling of methane is more relevant for Astoria Canyon runs. The largest difference in net transport compared to AST is for DIC (Barkley is 55% of AST).

As stated earlier in this section, the maximum net cross-shelf tracer transport occurs when the maximum body forcing is reached around day 3, during the time dependent phase of canyon-induced upwelling. We look at this maximum (or minimum for oxygen) in tracer transport because it will be important to explain the near bottom tracer distribution later. As with the mean net transport, we report the maximum transport, the canyon contribution and the relative value with respect to AST (Table 3 columns 6 to 8). As with the mean net transport, the highest maximum occurs for AST, followed by ARGO, PATH and BAR but the canyon contribution is larger than for the mean, which is consistent with the fact that the peak is induced by the canyon. The maximum follows similar patterns to the mean except for methane which shows more discrepancy between ARGO, BAR and PATH.

3.3 On-shelf tracer distribution

In a previous study, we described the distribution of tracer caused by canyon-induced upwelling for a linear profile (RA2019). We found that tracer is upwelled up onto the shelf by canyon-induced upwelling of water and through vertical mixing. Water upwells on the downstream side of the canyon, near the head and close to the shelf bottom carrying deeper tracer with it. The upwelled water, having higher density, spills onto the downstream shelf forming a pool of water. In this study we see that the pool forms a dense, nutrient-rich, oxygen-depleted region on the downstream shelf. Above this layer, tracer is being exported on-shelf near the canyon by the flow that veers towards the canyon head and off-shelf by off-shelf water transport balancing shelf-break and canyon-induced upwelling.

3.3.1 Bottom effect

The signature of the upwelled water is found close to shelf bottom, around the canyon rim (canyon-upwelled water) and along the shelf break (shelf-break upwelling) and is characterized by higher concentrations than background values (Animation S1, Figure 5a,b). Tracer that is upwelled onto the shelf through the canyon forms a ‘pool’ near shelf bottom, downstream of the canyon. We define this pool as the cells, at shelf bottom, where tracer concentration is larger or equal to that initially at shelf break depth ($C \geq C_{sb}$). The horizontal extent of the pool at shelf bottom (bounded by $C=C_{sb}$) is larger for all Astoria Canyon tracers than for Barkley Canyon tracers, because the amount of water upwelled is larger for Astoria Canyon and so more tracer is advected onto the shelf. The ARGO run has smaller pools than AST for the same reason.

At the peak of the time dependent phase (day 3), the pool builds up around the canyon rim, mostly on the downstream side and head of the canyon, with the highest concentration close to the head (Animation S1, Figure 5 a, b). As with water, this pool grows faster during the time-dependent phase and slower during the advective phase of upwelling (Figure 6 a, c). Even though the pool is formed during the time-dependent phase, it is maintained during the advective phase and generally continues to grow. The pool is a feature of all tracers and its horizontal extension strongly depends on the initial tracer profile and canyon bathymetry. Methane on Astoria Canyon’s shelf has the largest pool, spanning an area 47 times the canyon area. Oxygen has a pool spanning

Table 4. *Pool Area and Concentration*

Tracer	A_{pool}/A_{can} at day 9	Max (A_{pool}/A_{can})	Mean C_{pool} at day 9	max C_{pool}	max ΔC_{pool} (%)
AST Oxy	35.3	35.3	96.2	86.7	-16.7
ARGO Oxy	20.4	20.4	95.5	90.8	-12.7
BAR Oxy	1.9	6.5	79.4	79.4	-6.4
PATH Oxy	5.7	11.0	75.7	75.7	-10.7
AST Met	47.3	47.3	25.6	32.4	85.4
ARGO Met	32.9	32.9	24.9	29.6	69.2
BAR Met	0.6	5.0	38.6	38.9	7.1
PATH Met	1.2	7.5	38.4	39.2	8.1
AST DIC	16.8	21.8	2.23×10^3	2.24×10^3	1.0
ARGO DIC	10.2	11.6	2.23×10^3	2.24×10^3	0.8
BAR DIC	2.7	9.4	2.25×10^3	2.25×10^3	0.3
PATH DIC	7.8	15.8	2.25×10^3	2.25×10^3	0.4

Note. Pool area normalized by canyon area at day 9, maximum pool area, mean and maximum pool concentration, and maximum change in concentration from initial concentration for selected tracers. Concentration units are $\mu\text{mol/kg}$, $n\text{M}$, $\mu\text{mol/kg}$. Results for all tracer available in Table S2.

about 37 times the area of Astoria Canyon while DIC has a smaller pool of 16 times Astoria Canyon's area. For oxygen, the pool constitutes a low oxygen region. Maximum pool area and pool area at day 9 are reported in Table 4 columns 1 and 2.

The vertical extent of the pool, delimited by the contour of value 1 ($C/C_{sb} = 1$) considering the concentration normalized by the initial tracer concentration at shelf break depth, is between 10 m and 40 m above the shelf bottom. For the linear tracer over Astoria Canyon, deviations from the initial tracer profile are identified up to 40 m above shelf bottom near the canyon head (virtual station S1, Figure 5c). Stations farther away from the head (S2, S3) show deviations up to 25 m above shelf bottom. In BAR, deviations reach up to 20 m (Figure 5 d). This suggests that there is a stronger bulging of

the pool near the canyon head for Astoria Canyon than for Barkley Canyon. All tracers follow a similar pattern and although the pool's vertical extension does not reach the euphotic zone (particularly important if the tracer is nitrate), the pool is relevant to the overall tracer inventory on the shelf (nutrients in general) and the demersal and benthic ecosystems.

The pool's mean concentration peaks around day 2.5, when the maximum forcing is being applied and from there, the pool's mean concentration decreases throughout the rest of the simulation (Figure 6 b, d). Maximum changes in concentration occur for methane over Astoria Canyon with a 70-85% increase from the initial concentration at shelf break (Table 4 column 5, Figure 6) and smallest changes are for DIC with less than 1%. Concentration of the oxygen pool decreases by 13-17% from the initial concentration at shelf break in Astoria Canyon runs and between 6-11% for Barkley Canyon runs.

3.3.2 *Near-surface effect on oxygen and nitrate*

Canyon-induced upwelling has a near surface signature. Profiles of oxygen and nitrate near the shelf break and downstream of the canyon (station S4) show a negative (oxygen) and positive (nitrate) anomaly near the surface with respect to their initial concentration profiles. This anomaly is larger than the bottom anomaly in the 'pool' at that station for both, Astoria Canyon and Barkley Canyon runs (Figure 5 g1, g2, h1, h2). This anomaly is also present in profiles at stations S1-S3 for Barkley Canyon and less so for Astoria Canyon.

3.4 Canyon-induced tracer upwelling

We identify water upwelled through the canyon by its concentration of linear tracer. Water that was originally below shelf break depth has a linear tracer concentration larger than the shelf break value (see section 2.4). We find there is a larger upwelling flux Φ (1) of water onto the shelf for Astoria Canyon runs than for Barkley Canyon runs (Figure 7a) and that the canyon effect is larger too (Figure 7c). For Astoria Canyon runs the water upwelling flux during the advective phase Φ is $8.36 \times 10^4 \text{ m}^3 \text{ s}^{-1}$ for AST and $4.77 \times 10^4 \text{ m}^3 \text{ s}^{-1}$ for ARGO, while the water upwelling flux for Barkley Canyon runs is $1.43 \times 10^4 \text{ m}^3 \text{ s}^{-1}$ for BAR and $2.18 \times 10^4 \text{ m}^3 \text{ s}^{-1}$ for PATH. The scaling estimate developed by Howatt and Allen (2013), predicts these values within 20%. Similarly, the upwelled

Table 5. Tracer Upwelling Flux and On-shelf Tracer Inventory

Tracer	$\Phi_{Tr}/10^9 \mu\text{mol s}^{-1}$	$(\mathcal{M} - \mathcal{M}_{nc})/10^{12} \mu\text{mol}$	$(\mathcal{M} - \mathcal{M}_{nc})/(\mathcal{M}_{nc} - \mathcal{M}_{nc0})$ (%)
AST Oxy	7.06±0.54	-2.57×10 ³	96.2
ARGO Oxy	3.97±0.62	-1.30×10 ³	47.9
BAR Oxy	1.13±0.33	-161.2	6.8
PATH Oxy	1.63±0.33	-282.4	10.9
AST Met	(2.79±0.31)×10 ⁻³	1.0	203.5
ARGO Met	(1.64±0.16)×10 ⁻³	0.5	109.4
BAR Met	(0.53±0.15)×10 ⁻³	0.1	7.8
PATH Met	(0.81±0.15)×10 ⁻³	0.1	11.5
AST DIC	187.55±16.44	3.49×10 ³	89.0
ARGO DIC	107.20±13.74	1.76×10 ³	44.0
BAR DIC	32.26±8.98	208.6	6.4
PATH DIC	49.17±8.97	360.5	10.1

Note. In column 2: Mean tracer upwelling flux [Φ_{Tr} in 2] for selected tracers during the advective phase (days 4-9), reported with 12-h standard deviations. In columns 3 and 4: Tracer inventory or anomaly of total tracer mass on shelf [see (3)] and percentage relative to no-canyon case. Results for all 10 tracers are available in Table S2.

tracer flux Φ_{Tr} (2) is quantified by summing the tracer flux through cells identified in the previous step (see section 2.4). Consistent with results for the water upwelling flux, tracer upwelling flux is larger for Astoria Canyon runs than for Barkley Canyon runs (Figure 7b). Tracer upwelling flux spans several orders of magnitude due to the very different concentrations of each tracer but for all tracers, Φ_{Tr} is largest for AST followed in descending order by ARGO, PATH, and BAR (Table 5, column 2).

We compare Φ_{Tr} during the advective phase to the upwelled water flux from the model Φ multiplied by the initial concentration at shelf break depth C_{sb} (Figure 7e). The quantity ΦC_{sb} reproduces the tracer flux within 20% for all tracers except methane, oxy-

gen and linear tracer (Figure 7f). The percent difference between Φ_{Tr} and ΦC_{sb} increases as a function of the initial tracer gradient (Figure 7e), normalized by a characteristic length scale ΔZ and the concentration at shelf break depth C_{sb} . This dependence will be explained in section 4.1.

The on-shelf tracer inventory or the total amount of tracer mass on the shelf (3) increases as the canyon upwells water and tracers onto the shelf, except for oxygen. Since oxygen concentration decreases with depth, the water upwelled by the canyon has lower oxygen concentrations than the water exported off-shelf at shallower depths. We compare the effect of the canyon in upwelling each tracer by looking at the difference and fractional contribution of the canyon at the end of the simulation (day 9) compared to the runs having a straight shelf break, i.e. runs with no-canyon bathymetry (columns 3 and 4, Table 5). For all tracers, the tracer inventory increases more for Astoria Canyon runs than for Barkley Canyon runs. The relative contribution of the canyon is largest in the AST run for all tracers (204-88%) followed by ARGO run (109-43%), PATH run (18-10%) and BAR (10-6%).

4 Scaling considerations

There are two main processes acting to transport tracer onto the shelf: mixing and advection. Submarine canyons are considered regions of enhanced mixing because their steep walls and axis facilitate the breaking of internal tides and waves (e.g. Carter & Gregg, 2002; Lee et al., 2009; Gregg et al., 2011; Waterhouse et al., 2017). There is numerical evidence that locally-enhanced mixing within a canyon can increase the tracer transport by up to 25% (RA2019). The upwelling flux that advects the tracer onto the shelf has been scaled by Allen and Hickey (2010) and Howatt and Allen (2013). In the following sections we quantify the tracer mass content that is advected by the upwelling flow and the extension of the pool formed by the advected tracer on the shelf.

4.1 Scaling tracer upwelling flux

In section 3.4 we found that the upwelling flux Φ_{Tr} is proportional to the product between the water flux Φ and the initial concentration at shelf-break depth, C_{sb} , with an error proportional to the vertical gradient of the tracer concentration evaluated at shelf break depth (Figure 7f). The rationale for approximating $\Phi_{Tr} \approx \Phi C_{sb}$ is that if

the tracer concentration is uniform, then the flux of tracer onto the shelf Φ_{Tr} is the flux of water upwelled onto the shelf Φ multiplied by the concentration of the water. Since the initial concentration is not uniform, the upwelling flux carries water with concentrations up to $C(H_h + Z)$, that is up to the concentration of the deepest water that upwells (Figure 8a). Allen and Hickey (2010) and Howatt and Allen (2013) identify the deepest isopycnal that upwells onto the shelf (Figure 8a). The depth of this isopycnal is $H_h + Z$, where H_h is the canyon-head depth, and Z is called the depth of upwelling, given by (Howatt & Allen, 2013)

$$\frac{Z}{D_h} = 1.8(\mathcal{F}_W R_L)^{1/2}(1 - 0.42S_E) + 0.05, \quad (4)$$

where $D_h = fL/N$ is a depth scale, the function $\mathcal{F}_w = R_W/(0.9 + R_W)$ is the tendency of the flow to follow isobaths and $R_W = U/fW_s$ is a Rossby number that uses the width at mid-length measured at shelf-break depth W_s as a length scale. The slope effect is encapsulated in the function $S_E = sN_0/f(\mathcal{F}_w/R_L)^{1/2}$, where s is the shelf slope ($s=2.30 \times 10^{-3}$ for the Astoria-like bathymetry, 4.54×10^{-3} for the Barkley-like bathymetry).

Then, the concentration that multiplies the water flux can be written as the concentration at shelf break depth C_{sb} plus the concentration ΔC between H_h and $H_h + Z$. This correction will be larger if the gradient within the canyon is larger because the difference in concentrations at depths $H_h + Z$ and H_h will be larger. If the initial tracer concentration decreases with depth then the concentration C_{sb} will overestimate the mean concentration of the water that is being upwelled and the correction ΔC then decreases the concentration of the upwelled water. We propose the scaling for Φ_{Tr} to be

$$\Phi_{Tr} \propto \Phi(C_{sb} + \Delta C). \quad (5)$$

The correction ΔC can be written in terms of its derivative with respect to depth z :

$$\Delta C = \int_{H_h+Z}^{H_h} \frac{\partial C}{\partial z} dz \quad (6)$$

$$\approx Z \partial_z C, \quad (7)$$

where $\partial_z C$ is the mean vertical gradient over H_h to $H_h + Z$. Substituting (7) in (5)

$$\frac{\Phi_{Tr}}{\Phi C_{sb}} = a_1 + \frac{b_1 Z}{C_{sb}} \partial_z C \quad (8)$$

where $a_1 = 0.98$ and $b_1 = 0.57$ are found as the best-fit, least squares parameters with a standard error of 0.025 from the model results (Figure 9a).

4.2 Scaling the pool's extension

The formation of the pool of upwelled tracer described in section 3.3.1 depends on the flux of tracers onto the shelf described above. Once on the shelf, the alongshelf current will help spread the pool further downstream.

Detection of the pool relies on the tracer concentration of the upwelled water and the tracer concentration of the water on the shelf being different. So, the size of the pool as defined in section 3.3.1 depends on how much tracer is upwelled onto the shelf through the canyon as well as on the background tracer distribution on the shelf. We will find a scale for the pool area by comparing the distribution of the tracer upwelled by the canyon compared to the background distribution of the tracer on the shelf. The size of the pool will then depend on the same parameters as the upwelling flux of tracer, Z and $\partial_z C$, and analogous parameters characterizing the background tracer distribution on the shelf (Figure 8b).

Vertical diffusive fluxes at the boundary of the pool are estimated to be between 100 and 1000 times smaller than the advective flux feeding the pool, considering a vertical eddy diffusivity of $10^{-5} \text{ m}^2\text{s}^{-1}$ as in the model and the tracer gradients found in the pool. Larger diffusivities could induce a significant impact the size and concentration of the pool. However, it is uncommon to find such high values of eddy diffusivity on the shelf sustained over several days.

Allen and Hickey (2010) scale the upwelling flux by $UFW_m Z$, where \mathcal{F} is similar to \mathcal{F}_W but uses the Rossby number $R_o = U/f\mathcal{R}$ where \mathcal{R} is the radius of curvature of the shelf break isobath upstream of the canyon and W_m is the width of the canyon at the mouth. In addition, we know the change in concentration is proportional to $Z\partial_z C$ from section 4.1. So the tracer flux into the pool from canyon upwelling is scaled by $UFW_m Z^2 \partial_z C$. The rate of change of the depth averaged tracer anomaly in the pool is that flux over A_{pool} , the area of the pool.

If there was no canyon-induced upwelling, the distribution of tracer on the shelf, close to the bottom, would only depend on bottom friction generating an upslope Ekman transport through a bottom boundary layer (BBL). Thermal wind balance would eventually bring the along-isobath flow to rest at the bottom, shutting down the BBL. This is known as the buoyancy arrest of a bottom Ekman layer (Brink & Lentz, 2010).

A cross-shelf length scale for the BBL is given by $\mathcal{L} = fU/(N\theta)^2$, where $\theta \ll 1$ is the slope angle (MacCready & Rhines, 1993). A corresponding vertical scale is given by $\mathcal{H} = \mathcal{L}\theta$. So, the depth of the BBL can be estimated as \mathcal{H} .

A shutdown timescale is given by $\tau_0 = f/(N\theta)^2$ (MacCready & Rhines, 1993) (More precise estimates for the buoyancy arrest time of an upwelling BBL are derived in Brink & Lentz, 2010). So the depth integrated rate of change of the background concentration can be estimated as

$$\Phi_{bg} \approx \frac{\mathcal{H}}{\tau_0} (H_s - H_h) \partial_z C_{bg}, \quad (9)$$

where $(H_s - H_h) \partial_z C_{bg}$ is analogous to ΔC and represents the background concentration on the shelf within the shelf pool. We can distinguish the pool where the pool anomaly is greater than the background anomaly so approximating them as equal

$$A_{pool} \propto \frac{UFW_m Z^2 \partial_z C \tau_0}{\mathcal{H}(H_s - H_h) \partial_z C_{bg}}. \quad (10)$$

Further, the slope $s = (H_s - H_h)/L$ and angle θ are related as $\theta \sim s$, and we can approximate the area of the canyon, A_{can} , as the area of a triangle of base W_m and height L . Substituting s , A_{can} , and the expressions for \mathcal{H} and τ_0 in (10)

$$A_{pool} \propto 2A_{can}\Pi. \quad (11)$$

where

$$\Pi = \frac{\mathcal{F}Z^2 \partial_z C}{(H_s - H_h)^2 \partial_z C_{bg}}. \quad (12)$$

The pool area is a function of the canyon area and the non-dimensional number Π that represents the competition between the tracer that is upwelled onto the shelf through the canyon, which depends on the initial gradient of the tracer below the shelf, and the background tracer distribution on the shelf.

The relationship between the maximum area of the pool during the simulation, A_{pool} , (Table 4) and Π (Figure 9b) as follows:

$$A_{pool} = a_2(2A_{can}\Pi) + b_2 \quad (13)$$

where $a_2 = 5.4$, $b_2 = -3.2 \times 10^8 \text{ m}^2$ are found as best-fit, least squares parameters with a standard error of 0.3 from the model results (Figure 9b).

5 Discussion

Tracer is upwelled onto the shelf through advection and mixing. Canyon induced tracer upwelling is dominated by advection-induced upwelling of water through the canyon. It has been shown that locally-enhanced vertical diffusivity within the canyon can increase canyon-induced water and tracer upwelling of a linear tracer by more than 25% (RA2019). In this study, we show that variations in the vertical gradient of the initial tracer profile can have an impact on the amount of tracer that is upwelled onto the shelf through the canyon, as well as on the final distribution of the tracer on the shelf.

Tracer upwelled onto the shelf through the canyon forms a pool on the downstream side of the canyon rim that extends along the shelf downstream and shoreward. The horizontal extent of this pool is different for each tracer and it increases inversely with the relative magnitude of the initial gradient of the profile above shelf break depth compared to the mean gradient below shelf break depth. Larger gradients bring up water with higher concentration than can then be mixed up on the shelf which takes longer to dilute to a value below the initial concentration at shelf break depth C_{sb} while being advected downstream. Given that the pool is bounded, by definition, by the contour $C = C_{sb}$, having larger concentrations upwelled onto the shelf allows for a larger pool. The area of the pool relative to the area of the canyon can be characterized by the non-dimensional number Π (12) that represents the ratio between the tracer that is upwelled onto the shelf through the canyon and the initial distribution of the tracer on the shelf.

Upwelled tracer flux is scaled as the product of the upwelling flux Φ and the concentration $C_{sb} + \Delta C$. The effect of the geometry of the tracer profile is to increase the amount of tracer upwelled onto the shelf compared to a uniform profile. The quantity ΔC is proportional to the mean gradient at the depth of upwelling. For a profile that increases with depth, a larger depth of upwelling allows water with higher concentration to be upwelled onto the shelf. Thus, the mass of tracer upwelled is larger. For profiles that have sharp changes (large gradients) within the depth of upwelling, the concentrations that are upwelled will also be larger.

5.1 Canyon-induced tracer distribution on the shelf

In a numerical study of the regional effect that three submarine canyons have on the circulation and upwelling on the Washington Shelf, Connolly and Hickey (2014) iden-

tified a similar feature to the pool. They found that upwelling near canyons has a more direct influence on near-bottom water over the shelf when compared to runs with uniform bathymetry (without the canyons).

Another example of the near shelf bottom influence of submarine canyons is the contribution of the Murray Canyon Group to the formation of a cold and nutrient-rich water pool on the shelf of the eastern Great Australian Bight. Using numerical simulations, (Kämpf, 2007) showed a link between the formation of the pool and upwelling in the canyons, and estimated that the canyons contribute 72% of the volume and 81% of the nitrate in the pool. Our simulations show that during the advective phase of one upwelling event (days 4-9), Astoria Canyon contributes 30% of the nitrate, 42% of the methane and 61% of the DIC transported onto the shelf, while Barkley Canyon contributes with about 8% nitrate, 7% of the methane and 19% of the DIC, both when using realistic stratification (Table 5).

5.2 Significance to the near-bottom carbon system

The presence of corrosive, oxygen-depleted waters near the shelf bottom is common in upwelling systems. However, in the past 10 years this water has been reaching shallower depths and covering larger areas than normal on the West Coast of North America (Feely et al., 2008). Under a changing climate, the occurrence of these waters can be more frequent and in larger volumes than before. In our model, the canyons contribute between 19-68% of all the DIC that is transported onto the shelf during the advective phase of upwelling. By day 9, the DIC inventory on the Astoria Canyon shelf had increased between $1.7\text{-}3.5 \times 10^9$ mmol relative to the no canyon case while Barkley Canyon upwelled $0.2\text{-}0.4 \times 10^9$ mmol DIC when using linear and realistic stratifications, respectively. Considering the realistic stratification cases, the increase in DIC and total alkalinity relative to the no-canyon cases in the pool of upwelled water corresponds to a decrease in pH of 0.1 for Astoria canyon close to the canyon head and 0.04 for Barkley Canyon (station S1 in Figure 5e). Downstream of the canyon (S2 and S3) these changes are 0.03-0.06 for Astoria Canyon and 0.02-0.03 for Barkley Canyon. Closer to the shelf break (S4), the decrease in pH is 0.02 and 0.01 for Astoria Canyon and Barkley Canyon, respectively. To calculate the equivalent pH of the system we used MOCSY 2.0, which is open source collection of Fortran 95 routines to model ocean carbonate system thermodynamics (Orr & Epitalon, 2015).

5.3 Significance to nutrient upwelling

Although the near-bottom pool does not reach the euphotic zone (particularly important if the tracer is nitrate), the pool is relevant to the overall tracer inventory on the shelf (nutrients in general) and the demersal and benthic ecosystems.

Connolly and Hickey (2014) estimated that canyon-exported nitrate onto the shelf after 2 months during an upwelling season can be about $1.0\text{--}2.3 \times 10^7$ kg NO_3^- . We found that after a single, albeit strong, upwelling event (9 days), Astoria Canyon can increase the total inventory of nitrate mass on the shelf by 1.1 to 2.2×10^7 kg NO_3^- and Barkley Canyon by 1.4 to 2.4×10^6 kg NO_3^- compared to a straight shelf case. If we consider a 60-day upwelling period, then the canyon contribution to the tracer inventory could be up to 1.5×10^8 kg NO_3^- for Astoria canyon and up to 1.6×10^7 kg NO_3^- for Barkley Canyon. Using the linear tracer, which was used to do the same calculation in RA2019, the nitrate inventory contribution for Astoria Canyon is $0.7\text{--}1.3 \times 10^7$ and for Barkley Canyon $1.0\text{--}2.0 \times 10^6$ kg NO_3^- . So, using the realistic initial profile of nitrate represents an increase of 40% and 17-28%, respectively over using the linear tracer.

5.4 Scaling limitations

The off-shore and vertical position of the slope jet with respect to the canyon plays an important role in determining the dynamics in the canyon. (Jordi et al., 2005) numerically studied the impact of the jet's position relative to the canyon. They find that a jet closer to the canyon head generates stronger cross-shelf exchange. Based on that, we speculate that when the shelf jet is closer to the canyon head, the cross-shelf exchange of tracers will be enhanced and consequently, the pool will be larger.

Relaxation and downwelling events are common during the upwelling season in the California Current System (B. Hickey, 1998) and an upwelling event preconditions the tracer distribution on the shelf for consequent upwelling events. The pool forms mostly during the strongest part of the forcing event. So the difference between the advective phase and spin down of the current does not impact significantly the size of the pool. Once a pool is formed, further upwelling events increase the size and mean concentration on the pool region but the timing between events is important.

Poleward flow events, like the ones generated by local storms, may cause canyon-induced downwelling. These events will likely dilute the pool depending of their intensity and timing with respect to the generating upwelling event. Even if the downwelling event dilutes the pool, a large portion of the upwelled tracer remains on the shelf. This result suggests that having a succession of upwelling, relaxation, and downwelling events can still allow for the total tracer mass to build up on the shelf during the upwelling season. However, the persistence of the pool will be governed by the frequency and spacing between upwelling events and the strength of reversals in the alongshelf current.

5.5 Summary

1. Tracer upwelling induced by a submarine canyon depends on the amount of water upwelled but also on the vertical gradient of the initial tracer profile near shelf break depth and through the depth of upwelling. The error from approximating the canyon-induced tracer flux as the upwelling flux of water multiplied by the initial concentration of the tracer at shelf break depth as has been done previously, can be as large as 40%.
2. The canyon modifies the distribution of tracers on the shelf. During a canyon-induced upwelling event, a pool of dense water with low oxygen, high DIC and nutrients is formed on the shelf downstream of the canyon, near the bottom. This pool can be as large as 40 times the canyon area for Astoria Canyon and 15 times the canyon area for Barkley Canyon. The concentration of tracer within the pool can be up to 1.5 times that initially at shelf break depth, but the maximum value depends on the specific tracer.
3. Pool area is a function of the on-shelf canyon-induced tracer flux and the background tracer distribution on the shelf. The pool will be easily detected if more tracer is upwelled onto the shelf or if the initial tracer gradient on the shelf is small relative to that below shelf break depth.

Acknowledgments

We thank T. Jarníková for assistance using MOCSY, D. Capelle for providing methane and nitrous-oxide profiles, D. Sheinbaum and the UBC Canyons Group for fruitful discussions, and three anonymous reviewers whose suggestions helped improve this manuscript. Computing power was provided by WestGrid and Compute Canada. This work was funded

by a CONACYT scholarship and UBC through a 4-yr fellowship to KRM and NSERC
Discovery Grant RGPIN-2016-03865 to SEA. The model configuration and postprocess-
ing scripts can be consulted from our repository at [https://bitbucket.org/canyonsubc/
initial_profiles_paper](https://bitbucket.org/canyonsubc/initial_profiles_paper). Model output can be downloaded from the UBC Research
Data Collection, DOI pending.

References

- Allen, S. E. (1996). Topographically Generated, Subinertial Flows within A Finite Length Canyon. *J. Phys. Oceanogr.*, *26*, 1608–1632. doi: 10.1175/1520-0485(1996)026<1608:TGSFWA>2.0.CO;2
- Allen, S. E., & Durrieu de Madron, X. (2009). A review of the role of submarine canyons in deep-ocean exchange with the shelf. *Ocean Sci.*, *6*, 1369–1406. doi: 10.5194/osd-6-1369-2009
- Allen, S. E., & Hickey, B. M. (2010). Dynamics of advection-driven upwelling over a shelf break submarine canyon. *J. Geophys. Res.*, *115*(C8), C08018. doi: 10.1029/2009JC005731
- Allen, S. E., Vindeirinho, C., Thomson, R. E., Foreman, M. G., & Mackas, D. L. (2001). Physical and biological processes over a submarine canyon during an upwelling event. *Can. J. Fish. Aquat. Sci.*, *58*(4), 671–684. doi: 10.1139/f01-008
- Battisti, D. S., & Hickey, B. M. (1984). Application of remote wind-forced coastal trapped wave theory to the Oregon and Washington coasts. *Journal of Physical Oceanography*, *14*(5), 887–903. doi: 10.1175/1520-0485(1984)014<0887:AORWFC>2.0.CO;2
- Bianucci, L., Denman, K. L., & Ianson, D. (2011). Low oxygen and high inorganic carbon on the Vancouver Island Shelf. *J. Geophys. Res. Oceans*, *116*(7), 1–20. doi: 10.1029/2010JC006720
- Breitburg, D., Levin, L. A., Oschlies, A., Grégoire, M., Chavez, F. P., Conley, D. J., ... Zhang, J. (2018). Declining oxygen in the global ocean and coastal waters. *Science*, *359*(6371). doi: 10.1126/science.aam7240
- Brink, K. H. (1998). Deep-sea forcing and exchange processes. In K. H. Brink & R. E. E. Robinson (Eds.), *The global coastal ocean: Processes and methods* (Vol. 10, p. 151167). John Wiley & Sons.

- 766 Brink, K. H. (2006). Coastal-trapped waves with finite bottom friction. *Dyn. Atmos.*
767 *Oceans*, *41*, 172–190. doi: 10.1016/J.DYNATMOCE.2006.05.001
- 768 Brink, K. H., & Lentz, S. J. (2010). Buoyancy arrest and bottom ekman transport.
769 part i: Steady flow. *Journal of Physical Oceanography*, *40*(4), 621–635. doi: 10
770 .1175/2009JPO4266.1
- 771 Capelle, D. W., & Tortell, P. D. (2016). Factors controlling methane and nitrous-
772 oxide variability in the southern British Columbia coastal upwelling system.
773 *Mar. Chem.*, *179*, 56–67. doi: 10.1016/j.marchem.2016.01.011
- 774 Carter, G. S., & Gregg, M. C. (2002). Intense, Variable Mixing near the Head of
775 Monterey Submarine Canyon. *J. Phys. Oceanogr.*, *32*, 3145–3165. doi: 10
776 .1175/1520-0485(2002)032<3145:IVMNTH>2.0.CO;2
- 777 Connolly, T. P., & Hickey, B. M. (2014). Regional impact of submarine canyons dur-
778 ing seasonal upwelling. *J. Geophys. Res. Oceans*, *119*, 953–975. doi: 10.1002/
779 2013JC009452
- 780 Connolly, T. P., Hickey, B. M., Geier, S. L., & Cochlan, W. P. (2010). Processes
781 influencing seasonal hypoxia in the northern california current system. *J. Geo-*
782 *phys. Res. Oceans*, *115*(C3). doi: 10.1029/2009JC005283
- 783 Dawe, J. T., & Allen, S. E. (2010). Solution convergence of flow over steep topogra-
784 phy in a numerical model of canyon upwelling. *J. Geophys. Res. Oceans*, *115*,
785 1–13. doi: 10.1029/2009JC005597
- 786 De Leo, F. C., Smith, C. R., Rowden, A. A., Bowden, D. A., & Clark, M. R.
787 (2010). Submarine canyons: hotspots of benthic biomass and productiv-
788 ity in the deep sea. *P. Roy. Soc. Lond. B Bio*, *277*(1695), 2783–92. doi:
789 10.1098/rspb.2010.0462
- 790 Dinniman, M. S., & Klinck, J. M. (2002). The influence of open versus periodic
791 alongshore boundaries on circulation near submarine canyons. *J. Atmos.*
792 *Oceanic Technol.*, *19*, 1722–1737. doi: 10.1175/1520-0426(2002)019<1722:
793 TIOOVP>2.0.CO;2
- 794 Feely, R. A., Sabine, C. L., Hernandez-Ayon, J. M., Ianson, D., & Hales, B. (2008).
795 Evidence for upwelling of corrosive “acidified” water onto the continental shelf.
796 *Science*, *320*(5882), 1490–1492. doi: 10.1126/science.1155676
- 797 Fernandez-Arcaya, U., Ramirez-Llodra, E., Aguzzi, J., Allcock, A. L., Davies, J. S.,
798 Dissanayake, A., ... Van den Beld, I. M. J. (2017). Ecological Role of Subma-

- rine Canyons and Need for Canyon Conservation: A Review. *Front. Mar. Sci.*,
 4, 1–26. doi: 10.3389/fmars.2017.00005
- Freeland, H. J., & Denman, K. L. (1982). A topographically controlled upwelling
 center off Vancouver Island. *J. Mar. Res.*, 40, 1069–1093.
- Gent, P. R., & McWilliams, J. C. (1990). Isopycnal Mixing in Ocean Circulation
 Models. *J. Phys. Oceanogr.*, 20, 150–155. doi: 10.1175/1520-0485(1990)
 020<0150:IMIOCM>2.0.CO;2
- Gregg, M. C., Hall, R. A., Carter, G. S., Alford, M. H., Lien, R.-C., Winkel, D. P.,
 & Wain, D. J. (2011). Flow and mixing in Ascension, a steep, narrow canyon.
J. Geophys. Res., 116, C07016. doi: 10.1029/2010JC006610
- Harris, P. T., Macmillan-lawler, M., Rupp, J., & Baker, E. K. (2014). Geomorphol-
 ogy of the oceans. *Mar. Geol.*, 352, 4–24. doi: 10.1016/j.margeo.2014.01.011
- Hickey, B. (1998). Coastal oceanography of western north america from the tip of
 Baja California to Vancouver island. In A. Robinson & K. Brink (Eds.), *The
 sea. coastal segment (18,e)* (Vol. 11, pp. 345–93). John Wiley & Sons, Inc.
- Hickey, B. M. (1989). Patterns and processes of shelf and slope circulation. In
 M. R. Landry & B. M. E. Hickey (Eds.), *Coastal oceanography of washington
 and oregon* (Vol. 47, pp. 41–115). Elsevier Science.
- Hickey, B. M. (1995). Coastal Submarine Canyons. In J. Müller & D. Henderson
 (Eds.), *Topographic effects in the ocean, 'aha huli'ka'a* (pp. 95–110). Hawaiian
 Winter Workshop, University of Hawaii at Manoa.
- Hickey, B. M. (1997). The Response of a Steep-Sided, Narrow Canyon to Time-
 Variable Wind Forcing. *J. Phys. Oceanogr.*, 27, 697–726. doi: 10.1175/1520-
 0485(1997)027<0697:TROASS>2.0.CO;2
- Hickey, B. M., & Banas, N. S. (2003). Oceanography of the U.S. Pacific Northwest
 coastal ocean and estuaries with application to coastal ecology. *Estuaries*, 26,
 1010–1031. doi: 10.1007/BF02803360
- Howatt, T. M., & Allen, S. E. (2013). Impact of the continental shelf slope on up-
 welling through submarine canyons. *J. Geophys. Res. Oceans*, 118, 5814–5828.
 doi: 10.1002/jgrc.20401
- IPCC. (2013). *Climate change 2013: The physical science basis. contribution of
 working group i to the fifth assessment report of the intergovernmental panel
 on climate change.* Cambridge, United Kingdom and New York, NY, USA:

- Cambridge University Press. doi: 10.1017/CBO9781107415324
- Jordi, A., Orfila, A., Basterretxea, G., & Tintoré, J. (2005). Shelf-slope exchanges by frontal variability in a steep submarine canyon. *Progress in Oceanography*, 66(2-4), 120–141. doi: 10.1016/j.pocean.2004.07.009
- Kämpf, J. (2007). On the magnitude of upwelling fluxes in shelf-break canyons. *Cont. Shelf Res.*, 27, 2211–2223. doi: 10.1016/j.csr.2007.05.010
- Kämpf, J. (2010). On preconditioning of coastal upwelling in the eastern Great Australian Bight. *J. Geophys. Res. Oceans*, 115(C12071), 1–11. doi: 10.1029/2010JC006294
- Kämpf, J. (2018). On the Dynamics of CanyonFlow Interactions. *Journal of Marine Science and Engineering*, 6(4), 129. doi: 10.3390/jmse6040129
- Keller, A. A., Ciannelli, L., Wakefield, W. W., Simon, V., Barth, J. A., & Pierce, S. D. (2017). Species-specific responses of demersal fishes to near-bottom oxygen levels within the California Current large marine ecosystem. *Mar. Ecol. Prog. Ser.*, 568, 151–173. doi: 10.3354/meps12066
- Klinck, J. M. (1996). Circulation study near submarine canyons : A modeling study. *J. Geophys. Res.*, 101, 1211–1223. doi: 10.1029/95JC02901
- Klymak, J., Dewey, R. K., Allen, S. E., & Waterman, S. (2013). *Pathways 2013 MVP cruise report* (Tech. Rep.).
- Lee, I.-H., Lien, R.-C., Liu, J. T., & Chuang, W.-s. (2009). Turbulent mixing and internal tides in Gaoping (Kaoping) Submarine Canyon, Taiwan. *J. Mar. Sys.*, 76, 383–396. doi: 10.1016/j.jmarsys.2007.08.005
- MacCready, P., & Rhines, P. B. (1993). Slippery bottom boundary layers on a slope. *Journal of Physical Oceanography*, 23(1), 5–22. doi: 10.1175/1520-0485(1993)023<0005:SBBLOA>2.0.CO;2
- Marshall, J., Hill, C., Perelman, L., & Adcroft, A. (1997). Hydrostatic, quasi-hydrostatic, and nonhydrostatic ocean modeling. *J. Geophys. Res.*, 102, 5733–5752. doi: 10.1029/96JC02776
- Mirshak, R., & Allen, S. E. (2005). Spin-up and the effects of a submarine canyon: Applications to upwelling in Astoria Canyon. *J. Geophys. Res.*, 110, C02013. doi: 10.1029/2004JC002578
- Orr, J. C., & Epitalon, J.-M. (2015). Improved routines to model the ocean carbonate system: mocsy 2.0. *Geoscientific Model Development*, 8(3), 485–499. doi:

- 10.5194/gmd-8-485-2015
- Puig, P., Palanques, A., & Martín, J. (2014). Contemporary Sediment-Transport Processes in Submarine Canyons. *Ann. Rev. Mar. Sci.*, 6(1), 53–77. doi: 10.1146/annurev-marine-010213-135037
- Ramos-Musalem, K., & Allen, S. E. (2019). The impact of locally-enhanced vertical diffusivity on the cross-shelf transport of tracers induced by a submarine canyon. *J. Phys. Oceanogr.*, 49, 561–584. doi: 10.1175/JPO-D-18-0174.1
- Redi, M. H. (1982). Oceanic Isopycnal Mixing by Coordinate Rotation. *J. Phys. Oceanogr.*, 12, 1154–1158. doi: 10.1175/1520-0485(1982)012<1154:OIMBCR>2.0.CO;2
- Santora, J. A., Zeno, R., Dorman, J. G., & Sydeman, W. J. (2018). Submarine canyons represent an essential habitat network for krill hotspots in a Large Marine Ecosystem. *Sci. Rep.*, 8(1), 7579. doi: 10.1038/s41598-018-25742-9
- She, J., & Klinck, J. M. (2000). Flow near submarine canyons driven by constant winds. *J. Geophys. Res.*, 105, 28,628–671,694. doi: 10.1029/2000JC900126
- Spurgin, J. M., & Allen, S. E. (2014). Flow dynamics around downwelling submarine canyons. *Ocean Sci.*, 10, 799–819. doi: 10.5194/os-10-799-2014
- Waterhouse, A. F., Allen, S. E., & Bowie, A. W. (2009). Upwelling flow dynamics in long canyons at low Rossby number. *J. Geophys. Res. Oceans*, 114(5), 1–18. doi: 10.1029/2008JC004956
- Waterhouse, A. F., Mackinnon, J. A., Musgrave, R. C., Kelly, S. M., Pickering, A., & Nash, J. (2017). Internal Tide Convergence and Mixing in a Submarine Canyon. *J. Phys. Oceanogr.*, 47, 303–322. doi: 10.1175/JPO-D-16-0073.1
- Whitney, F. A., Freeland, H. J., & Robert, M. (2007). Persistently declining oxygen levels in the interior waters of the eastern subarctic pacific. *Prog. Oceanogr.*, 75(2), 179 - 199. (Time Series of the Northeast Pacific) doi: 10.1016/j.pocean.2007.08.007
- Zhang, W. G., & Lentz, S. J. (2017). Wind-driven circulation in a shelf valley. Part I: Mechanism of the asymmetrical response to along-shelf winds in opposite directions. *J. Phys. Oceanogr.*, 47, 2927–2947. doi: 10.1175/JPO-D-17-0083.1

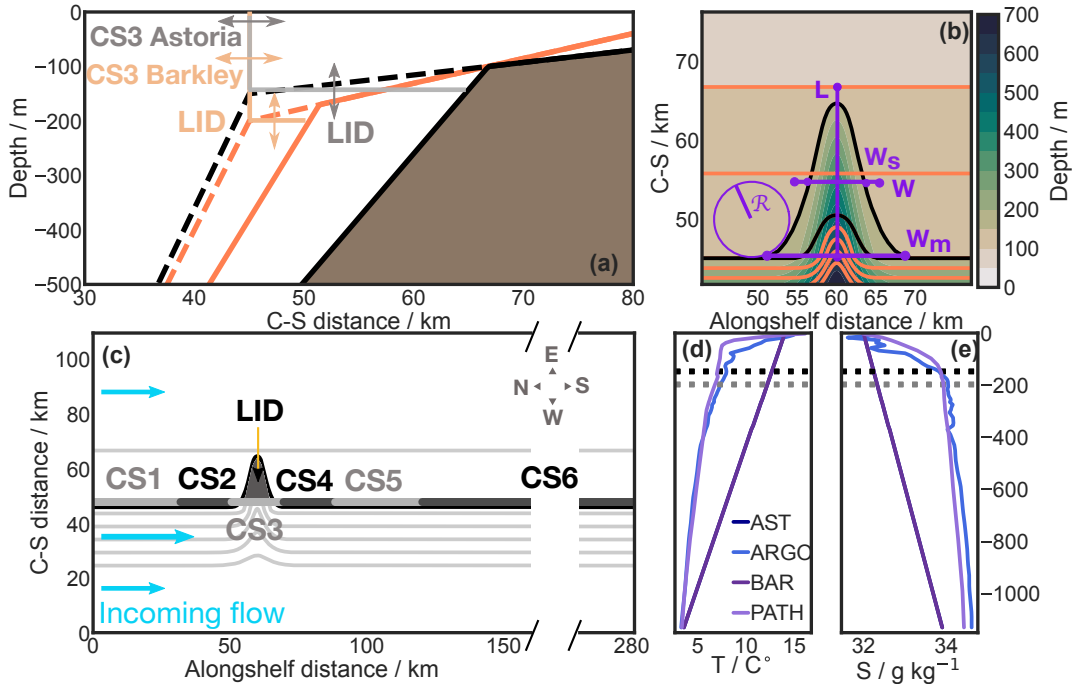


Figure 1. (a) Cross-shelf section showing depth profiles of the shelf (dashed) and canyon axis (solid) for Astoria-like (black) and Barkley-like (orange) bathymetries. Gray and peach lines correspond to the location of cross-sections CS3 and LID for Astoria-like and Barkley-like bathymetries, respectively. (b) Top view of Astoria-like (colormap) and Barkley-like (orange contours) bathymetries with shelf break isobaths in black. Dimensions of Astoria-like bathymetry in purple correspond to the cross-shelf length of the canyon from head to mouth $L=21.8$ km; $W_s=8.0$ km and $W_m=15.7$ km the alongshelf widths at mid-length at shelf break depth and mouth, respectively; and $R=4.5$ km, the upstream radius of curvature. Barkley Canyon dimensions are $L=6.4$ km, $W_s=8.3$ km, $W_m=13.0$ km and $R=5.0$ km. (c) Top view of the Astoria-like domain with depth contours 20, 100, 200, 400, 600, 800, 1000, 1200 m. The solid black line corresponds to the shelf break isobath along which we defined the cross-sections CS1-CS6 to calculate cross-shelf transport. The horizontal section LID was used to calculate vertical transport through the canyon. (d, e) Temperature and salinity profiles for all runs. Gray and black dotted lines indicate the shelf break depth for Barkley-like and Astoria-like bathymetries, respectively.

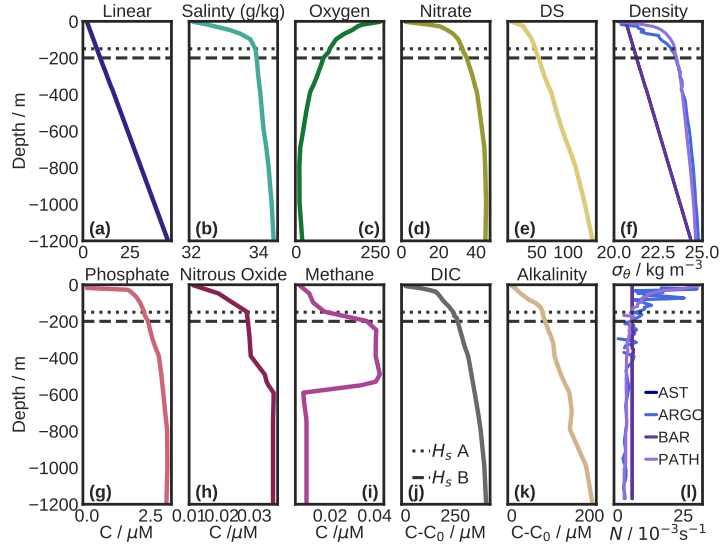


Figure 2. (a-e, g-k) Initial tracer profiles for all tracers used in the simulations. Dotted and dashed gray lines correspond to the shelf-break depth for the Astoria Canyon and Barkley Canyon bathymetries, respectively. (f) Initial density σ_θ and (l) buoyancy frequency N profiles for the four runs analysed in this paper.

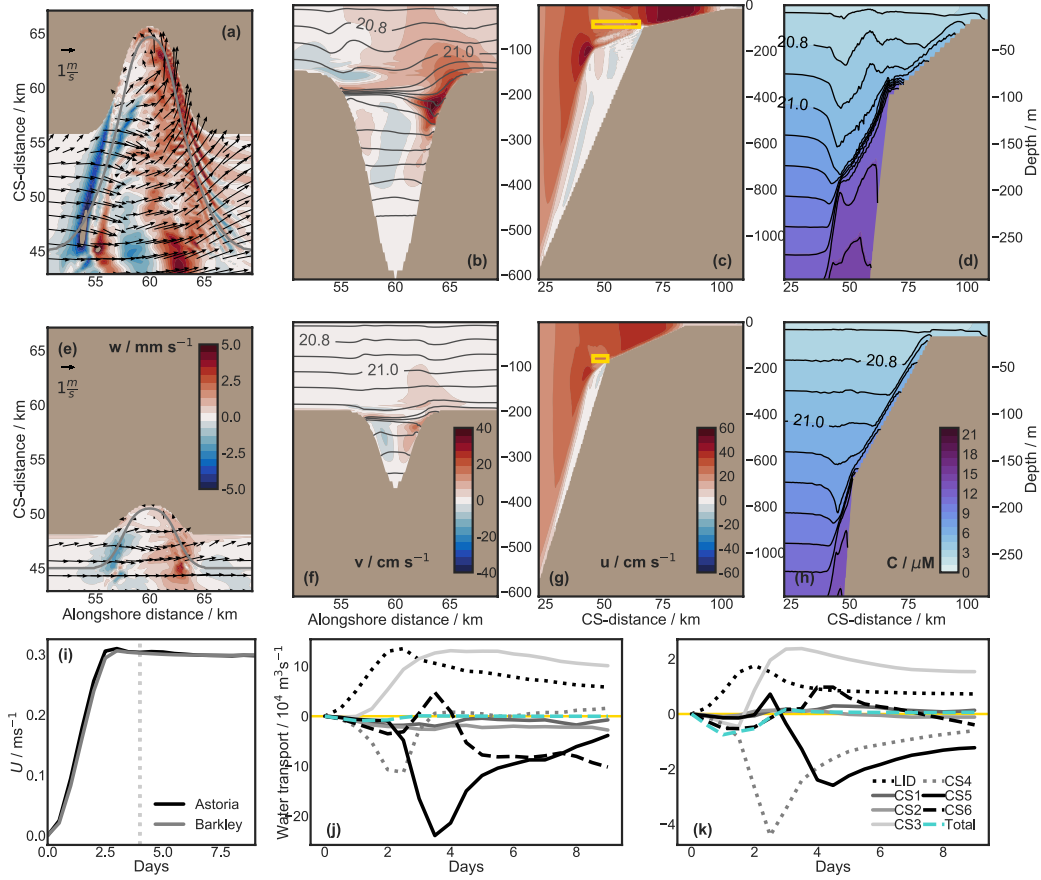


Figure 3. Advective phase (days 4-9) averages of (a, e) vertical velocity in color and horizontal velocity vectors at rim depth (mid-length depth), every 6th quiver is shown; (b, f) cross-shelf velocity in color (positive onto the shelf) and σ_θ contours every 0.1 kg m^{-3} at the canyon mouth; (c, g) alongshelf velocity at the canyon axis with positive velocities in the upwelling-favourable direction and (d, h) linear tracer concentration (color) and σ_θ contours every 0.1 kg m^{-3} along the canyon axis. Top and middle rows correspond to AST and BAR runs, respectively. (i) Along shelf velocity averaged over the yellow rectangles in c and g. (j, k) Water transport across sections CS1-CS6 and net CS water transport for Astoria Canyon (j) and Barkley Canyon (k) runs, note the difference in scale.

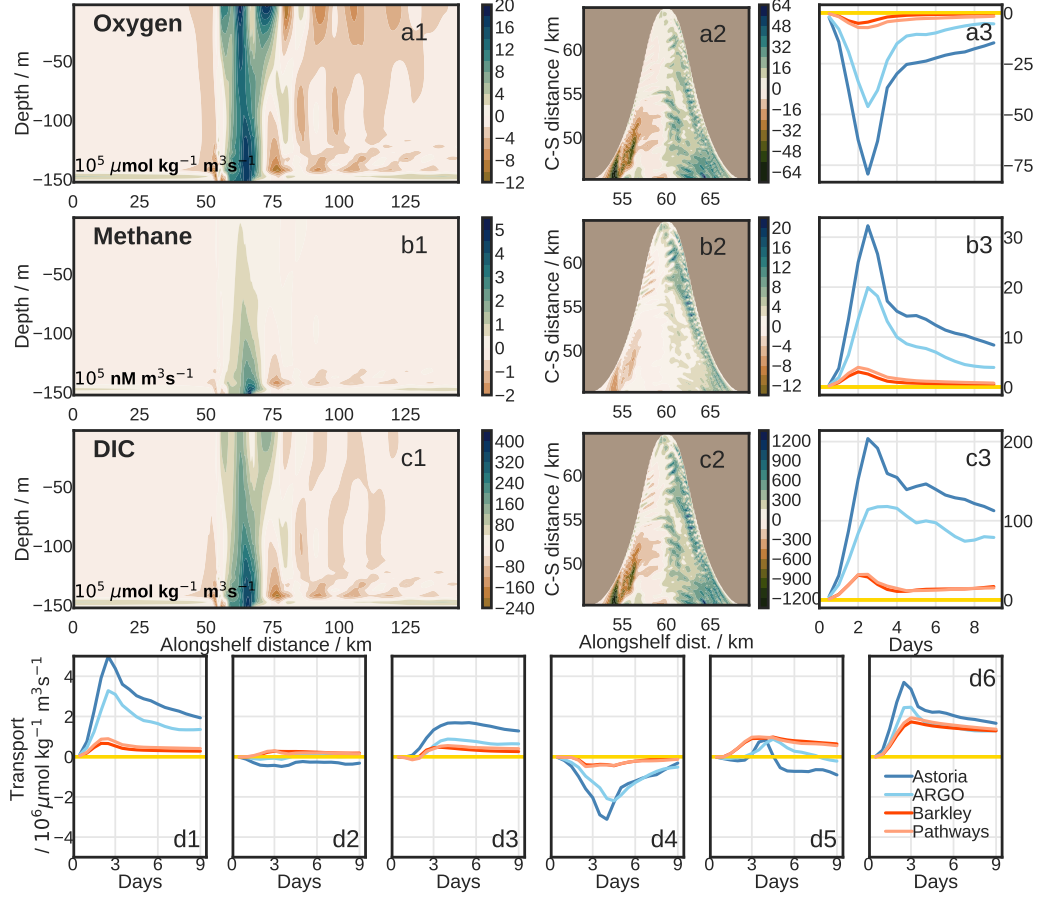


Figure 4. Mean cross-shelf (a1-c1) and vertical (a2-e2) transport of oxygen, methane and DIC (top to bottom) during the advective phase. (a3-c3) Canyon effect on the net cross-shelf transport of tracer during the simulation for all runs with the same units as given in left panel of each row. (d1-d6) Linear tracer transport through cross-sections LID, CS1+CS2, CS3,CS4,CS5+CS6 and net transport for all runs. Tracer transport onto the shelf occurs mostly above the canyon and through the canyon lid (canyon induced) and right above the shelf break (shelf-break upwelling).

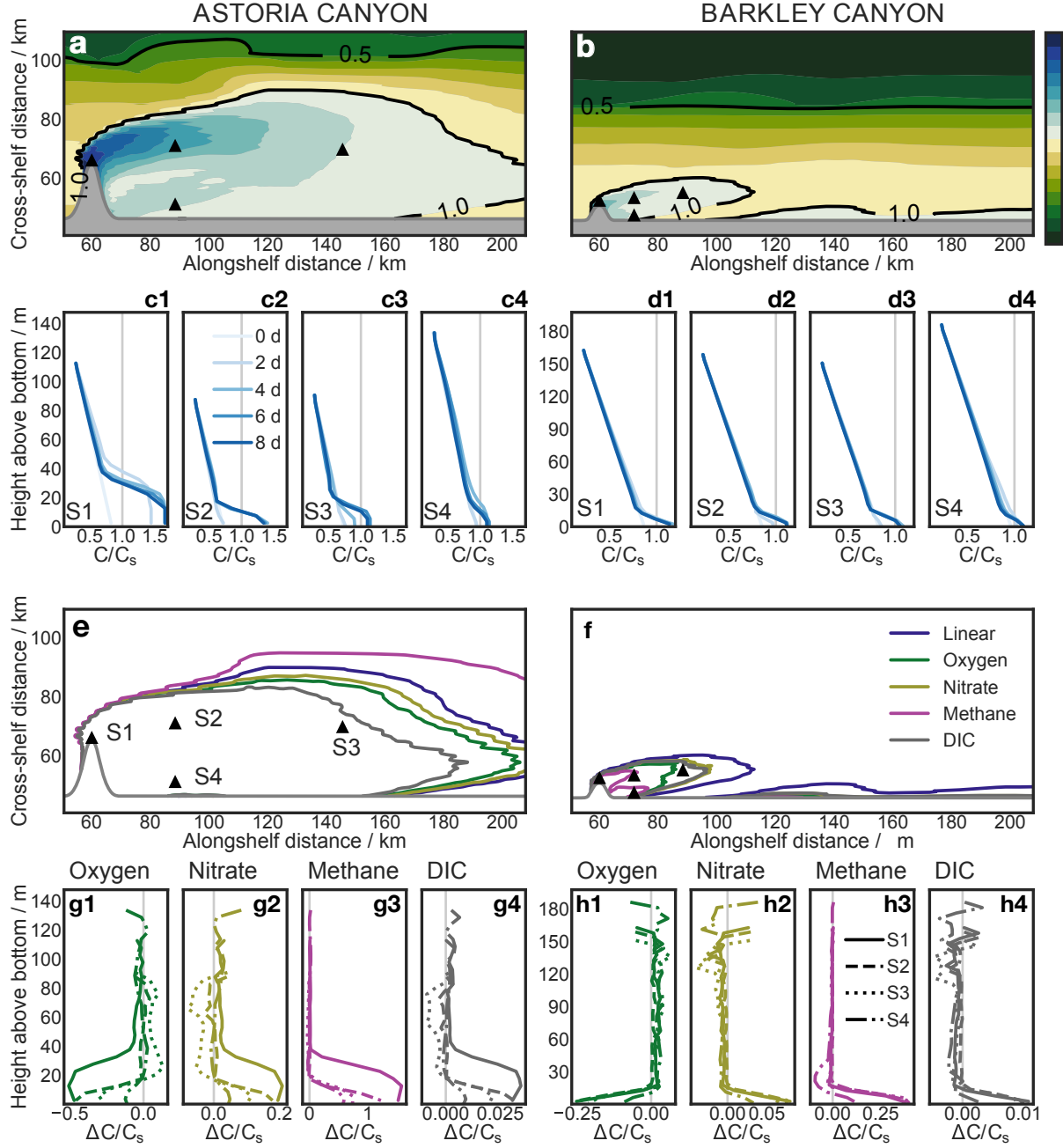


Figure 5. (a,b) The pool of upwelled linear tracer (contour value 1) shown as the mean bottom concentration of linear tracer during advective phase, C_{bottom} , normalized by the initial concentration at shelf break C_s . (c1-4, d1-4) Linear tracer profiles at days 0 through 8 at virtual stations S1-S4 (black triangles) show the near-bottom impact of the pool. (e, f) The pool boundaries for 5 different tracers (contour 1 C_{bottom}/C_s) show the dependence on the initial tracer profile. (g1-4, h1-4) Mean profiles showing changes from initial concentration ($\Delta C(z) = C(z) - C_0(z)$) at virtual stations S1-S4 during the advective phase.

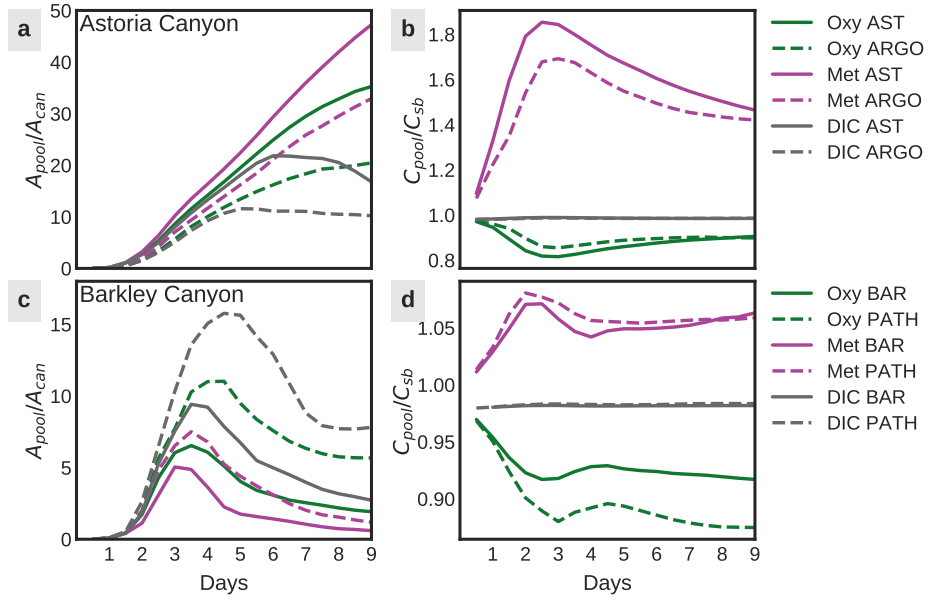


Figure 6. (a and c) Pool area normalized by canyon area increases faster during the time dependent phase (days 0-4) and is larger for AST and ARGO runs. (b and d) The mean pool concentration normalized by initial concentration at shelf-break depth C_{sb} is maximum (minimum for oxygen) around day 2.5 but stays higher than C_{sb} through out the simulation.

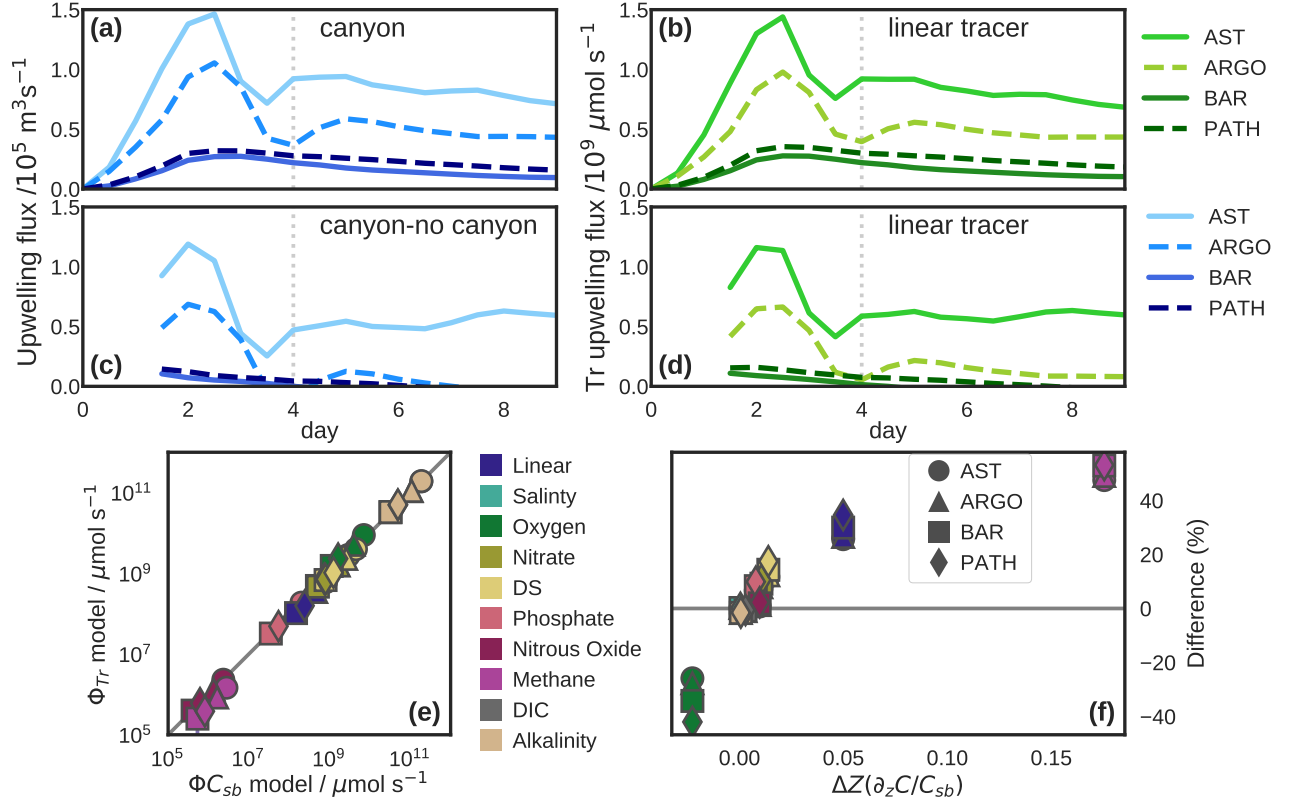


Figure 7. Flux of water (a) and flux of linear tracer (b) upwelled onto the shelf. The corresponding canyon contribution is calculated as the difference between canyon and no-canyon runs in (c) and (d). The dotted line marks the beginning of the advective phase of upwelling. (e) Upwelling flux of tracer from model output compared to the modelled water upwelling flux multiplied by the initial tracer concentration at shelf break depth ΦC_{sb} . Note that the marker for DIC is behind the marker for alkalinity. (f) Percentile error between quantities in (e) calculated as $(\Phi_{Tr} - \Phi C_{sb})/\Phi_{Tr}$ is a function of the tracer gradient near shelf break (local average 10 m) normalized by the averaging length $\Delta Z = 10$ m over C_{sb} .

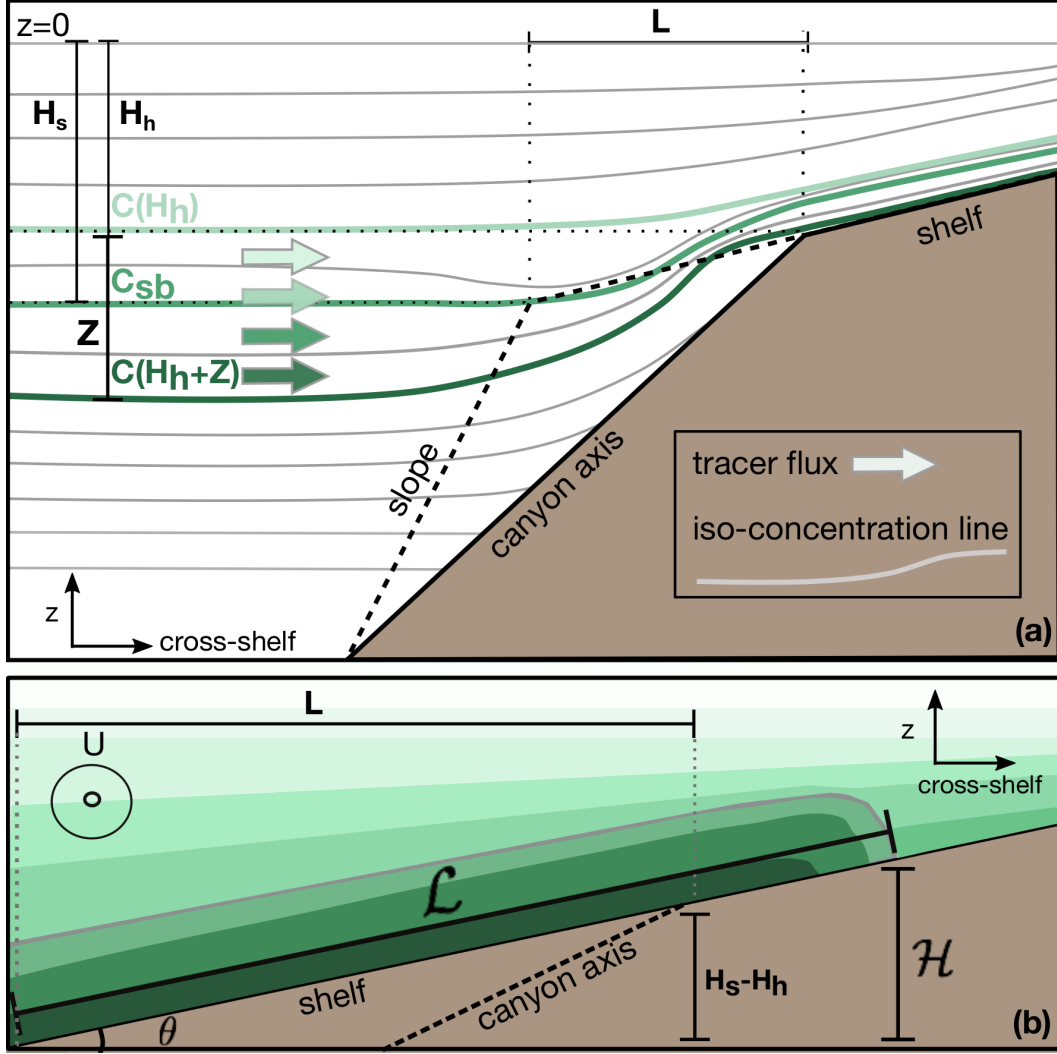


Figure 8. (a) The cross-shelf section at the canyon axis shows the tilting of isopycnals (gray solid lines) and iso-concentration lines (lines in shades of green) towards the canyon head during the upwelling event. Tracer upwelled by the upwelling flux (tracer flux) comes from depths between H_h and $H_h + Z$ and has a concentration between $C(H_h)$ and $C(H_h + Z)$. (b) Length scales used to scale the pool area are shown in a cross-shelf section of the shelf downstream of the canyon. The background pool, shown in tracer contours (shades of green, increasing with depth), has a cross-shelf length \mathcal{L} and associated vertical scale \mathcal{H} . The shelf slope is given by $\theta \ll 1$.

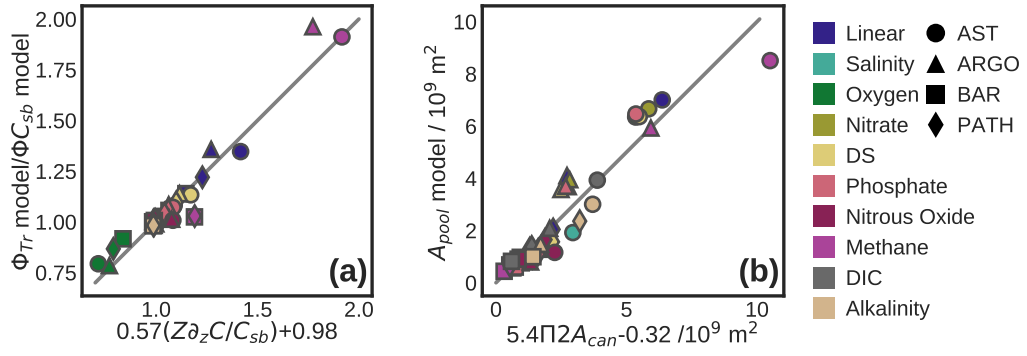


Figure 9. Scaling estimates for (a) tracer upwelling flux and (b) maximum pool area, equations (8) and (13), respectively. Tracer upwelling flux is proportional to upwelling flux and the initial tracer distribution within the canyon. The maximum pool area is a function of Π , a non-dimensional number given by the ratio between on-shelf canyon-induced tracer flux and the initial background tracer distribution on shelf.